Journal of Power Sources 192 (2009) 324–329

Contents lists available at ScienceDirect

Journal of Power Sources

journal homepage: www.elsevier.com/locate/jpowsour

Effect of boron doping in the carbon support on platinum nanoparticles and carbon corrosion

Chethan K. Acharya[a], Wei Li[a], Zhufang Liu[b], Gihan Kwon[a], C. Heath Turner[a,*], Alan M. Lane[a], David Nikles[b], Tonya Klein[a], Mark Weaver[c]

[a] Department of Chemical and Biological Engineering, The University of Alabama, Tuscaloosa, AL 35487, United States
[b] Department of Chemistry, The University of Alabama, Tuscaloosa, AL 35487, United States
[c] Department of Metallurgical and Materials Engineering, The University of Alabama, Tuscaloosa, AL 35487, United States

ARTICLE INFO

Article history:
Received 8 February 2009
Received in revised form 5 March 2009
Accepted 5 March 2009
Available online 19 March 2009

Keywords:
Platinum nanoparticles
Carbon
Boron-doped carbon
Stability
Corrosion

ABSTRACT

Carbon supported catalysts can lose their activity over a period of time due to the sintering of the nanometer-sized catalyst particles. The sintering of metal clusters on carbon supports can occur due to the weak interaction between the metal and the support and also due to the corrosion of carbon, especially in fuel cell electrocatalysts. The sintering may be reduced by increasing the interaction between the metal and the support and also by increasing the corrosion resistance of carbon supports. In an effort to mitigate the growth of the nanoparticles, carbon-substituted boron defects were introduced in the carbon lattice. The interaction between the Pt nanoparticles on the pure and boron-doped carbon supports was examined using X-ray photoelectron spectroscopy (XPS). The results indicate that the interaction between the Pt nanoparticles and the boron-doped carbon support was slightly stronger than the interaction between the Pt nanoparticles and the pure carbon support. Also, by using accelerated aging tests, the boron-doped system was found to be more resistant to carbon corrosion when compared to the pristine carbon-supported Pt catalyst.

1. Introduction

Metal nanoparticles such as Pt and Ru supported on carbon black are very common catalysts for various applications, ranging from reductive amination to fuel cell electrode catalysis [1–5]. The size and shape of the nanoparticles play important roles in determining the activity of the catalysts [6–12]. However, the deposited nanoparticles can grow in size over a period of time due to the thermally or electrochemically activated diffusion of the nanoparticles on the surface of the support [8,13]. When the particles collide they coalesce, resulting in a loss of particle surface area and concomitant loss of catalytic activity. The diffusion rate depends on the size and shape of the nanoparticles, and the physical and chemical environment under which the catalysts are used. For instance, in the presence of electrolytes, ions can accelerate the diffusion of the nanoparticles because the electrolytes weaken the interaction between the nanoparticles and the support [14,15]. In addition, Jensen et al. [16–18] have shown experimentally and computationally that one of the reasons for the diffusion of nanoparticles on perfect surfaces is the mismatch of the lattices of the nanoparticles and the substrates, and this mismatch can depend upon the size and shape of the nanoparticles. The diffusion of the nanoparticles also tends to increase with temperature [19–22].

The sintering of the nanoparticles, by either a coalescence mechanism (the entire cluster migrates on the support to form a larger cluster) or an Ostwald ripening mechanism (single atoms detach from smaller clusters and migrate to feed the growth of larger clusters), may be minimized by increasing the interaction between the metal and the support. This may be achieved by functionalizing the surface of the support or by creating various defects, such as steps, terraces, and vacancies [19,23–26]. Therefore, if appropriate support materials are identified, the activity of the catalysts could be prolonged.

Another issue related to the durability of the fuel cell catalysts is the corrosion of the carbon support. Carbon support corrosion reduces the distance between the metal nanoparticles and depletes the anchor sites for the nanoparticles, leading to their aggregation/dissolution. Besides, it can also lead to an increase in surface hydrophobicity that can decrease the gas transport in electrodes.

There are two proposed principle pathways for the carbon support corrosion [27]

$$C + 2H_2O = CO_2 + 4H^+ + 4e^-, \qquad 25\,^\circ C, \quad 0.207\,V \text{ vs. SHE} \qquad (1)$$

* Corresponding author at: Department of Chemical and Biological Engineering, The University of Alabama, Box 870203, Tuscaloosa, AL 35487, United States. Tel.: +1 205 348 1733; fax: +1 205 348 7558.
E-mail address: hturner@eng.ua.edu (C. Heath Turner).

0378-7753/$ – see front matter © 2009 Elsevier B.V. All rights reserved.
doi:10.1016/j.jpowsour.2009.03.020

$$C + H_2O = CO + 2H^+ + 2e^-, \quad 25\,^\circ C, \quad 0.518\,V \text{ vs. SHE} \qquad (2)$$

CO is thermodynamically unstable with respect to CO_2, and

$$CO + H_2O = CO_2 + 2H^+ + 2e^-, \quad -0.103\,V \text{ vs. SHE} \qquad (3)$$

The detailed mechanisms are not yet fully understood but are presumed to include parallel formation of surface and gaseous carbon oxides by disproportionation of oxygen functional groups [28].

Carbon support corrosion is a cause of degradation of the proton exchange membrane fuel cell (PEMFC) cathode, which generally operates in a potential window of 0.6–1 V. The anode of direct methanol fuel cell (DMFC) is also susceptible to carbon support corrosion because it operates around 0.4 V [29]. Carbon support corrosion causes irreversible cathode/anode catalysts degradation and should be suppressed or mitigated by using better supports. The review by Borup et al. [30] on the durability and degradation of the PEMFC discusses the novel support materials currently being investigated by others such as nanotubes, metal oxides, silicon, conducting polymers, conductive diamonds, and non-conductive whiskers. Conductive diamonds are synthesized by doping elements such as boron in the diamond lattice, which is an approach similar to our boron-doped carbon powders.

To address these issues, using first-principles density functional theory (DFT) calculations, we have previously shown that the presence of substitutional boron defects in carbon models (such as graphene and fullerenes) significantly increases the adsorption energies of Pt and Ru metal clusters when compared to pristine carbon models [31–33]. The binding energy per Pt and Ru atom on boron-doped carbon was greater by approximately 14 and 42 kcal mol^{-1}, respectively, than the binding energy of the metal atoms on pristine carbon.

To corroborate the DFT results of enhanced interaction of the Pt clusters with the boron-doped carbon when compared to the pure carbon, we have synthesized pure and boron-doped carbon black at a relatively mild temperature of 1000 °C and ambient pressure. Boron trichloride and benzene were used for the synthesis of boron-doped carbon, and only benzene was used for the synthesis of pure carbon. We then used these two materials as catalyst supports for Pt nanoparticles. Our procedure for synthesizing the amorphous carbons and the associated characterization needed to confirm the presence of substitutional boron in the carbon lattice has been reported earlier [34]. By changing the amount of boron trichloride in the feed gas during the synthesis procedure, we are able to change the amount of boron in the carbon black. The highest boron composition in carbon achieved by this method was 10.9%. However, in the present study, we are only using two samples as carbon supports for the Pt nanoparticles: (i) the pure carbon; and (ii) the boron-doped carbon with 8.5% boron in carbon (synthesized with a BCl_3:C_6H_6 feed ratio of 1.8:1). In this study, in addition to studying the interaction of Pt with the pure and boron-doped carbon using XPS, the carbon corrosion of the pure and boron-doped carbon is analyzed by accelerating the aging of the catalysts using potential cycling.

2. Experimental procedures

2.1. Synthesis of pure and boron-doped carbon

Boron trichloride and benzene were used for the synthesis of boron-doped carbon. The reaction was carried out at 1000 °C and 1 atmosphere in a 0.375 in. quartz tube reactor. The heat required for the reaction was provided by an Omegatite ceramic furnace encompassing the quartz tube reactor. There were two 0.125 in. quartz rods in the reaction zone for the carbon deposition. The downstream end of the reactor was connected to a neutralization tank which was filled with a NaOH solution to neutralize the HCl produced during the reaction, and the gases were vented out through an exhaust system.

The flow rates of the reactants were calculated assuming the following reaction to occur in the reactor:

$$5C_6H_6 + 6BCl_3 \rightarrow 6BC_5 + 18HCl + 6H_2 \qquad (4)$$

To produce pure carbon, C_6H_6 and He were fed into the reactor. To vary the composition of boron in the carbon samples, the reactions were carried out by changing the amount of BCl_3 in the feed stream. The reactants were fed into the reactor at 1000 °C and the reactions were allowed to continue until the reactor was blocked with carbon deposit. The feed to the reactor was stopped once this occurred and the products were cooked at 1000 °C for 5 min, then allowed to cool to room temperature. Doping was monitored using X-ray diffraction (XRD) and Raman spectroscopy, and boron content was estimated by XPS. Our procedure for the synthesis and characterization of the pure and boron-doped carbons can be found in the work of Burgess et al. [34]. In the present study, we are only using the pure carbon and the boron-doped carbon with 8.5% boron in carbon as supports for the Pt nanoparticles.

2.2. Synthesis of Pt nanoparticles

In order to synthesize the Pt nanoparticles, 390 mg of platinum acetylacetonate (97%, Aldrich), 780.0 mg of 1,2-hexadecanediol (90%, Aldrich) and 40.0 ml of diphenyl ether (70%, Acros Organic) were added into a 100 ml round flask equipped with a magnetic stirrer and a reflux condenser. The mixture was heated from room temperature to 110 °C, during which 2.0 ml of oleylamine (70%, Aldrich) and 2.0 ml of oleic acid (90%, Aldrich), used as capping agents, were introduced by a syringe. The mixture was then heated to 175 °C and was kept at this temperature for 1 h. Afterwards, the obtained black particle dispersion was allowed to cool down to 50 °C under N_2 atmosphere. The excess capping agents on the particle surface were removed by washing the particles with ethanol followed by centrifugation. Finally, the as-prepared particles were redispersed in hexane to make the Pt nanoparticle dispersion [35–38].

2.3. Loading the Pt nanoparticles onto a carbon support

100 mg of the as-prepared Pt nanoparticles dispersed in hexane were first mixed with 400 mg of carbon support (pristine carbon and boron-doped carbon). Particles were physically deposited on the carbon support by sonicating the resulting mixture for 2 h. The carbon-supported nanoparticle dispersion was then dried at 60 °C under an air atmosphere to evaporate the hexane. For catalytic activation of nanoparticles, the oleylamine and oleic acid bound to the particle surface were removed by heat treating the carbon-supported particles in a tube furnace at 400 °C for 3 h under an Ar/H_2 atmosphere (5% of H_2). The heat-treated Pt particles were mixed with deionized water and Nafion® solution (5 wt%, Aldrich) to make a Pt catalyst slurry (approximately 1 mg Pt ml^{-1}).

2.4. Analytical techniques

X-ray photoelectron spectra were collected with a Physical Electronics APEX surface analysis system with an Omicron EA125 hemispherical analyzer. Before the samples were analyzed, the XPS instrument was calibrated using a gold foil (Au $4f_{7/2}$: 83.99 eV) [39] after cleaning with a 5 kV Ar^+ ion sputtering gun with a Physical Electronics Model 11-066 Ion Gun Control. XPS measurements were acquired with a Mg Kα source at a take-off angle of 45°. Peaks shifts were corrected for charging using an adventitious C(1s) peak of 284.8 eV [34,40,41].

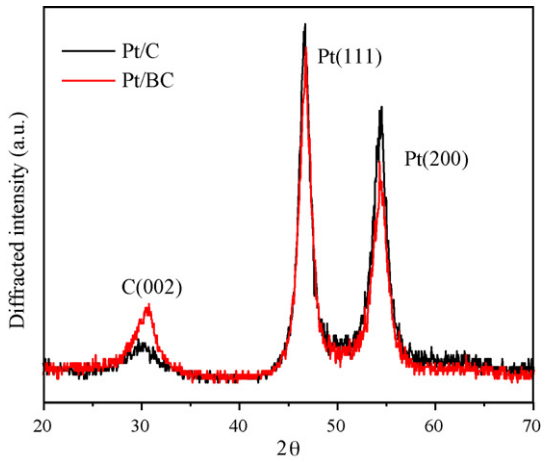

Fig. 1. XRD spectra of Pt nanoparticles on the pure carbon and the boron-doped carbon support.

X-ray diffraction measurements were made using a Bruker diffractometer using a Co Kα radiation (λ = 1.79026 Å). The acceleration voltage was 35 kV and the tube current was 40 mA. The samples were placed on a silicon slab for analysis.

Transmission electron microscopy (TEM) images of the samples were obtained on a FEI Tecnai F-20 200 kV transmission electron microscope. The TEM samples were made by placing several drops of dilute particle dispersion on carbon-coated copper TEM grids (400-mesh from Ted Pella, Inc.).

2.5. Accelerated aging studies

Potential cycling is a common accelerated degradation test for electrocatalysts of PEMFC. It was performed in a 0.5 M H_2SO_4 electrolyte with a bipotentiostat (AFCBP1, Pine Instrument) and a 150 ml three-electrode electrochemical cell (Pine Instrument). A mirror-ground GC rotating disk electrode (GC-RDE, 5 mm diameter, Pine Instrument) was polished using a 0.05 μm γ-alumina micropolish (Buehler LTD, No. 40-6365-006) on a microcloth PSA (Buehler LTD, 40-7212), followed in sequence by rinsing and ultrasonicating for 2 min in DI water before each usage. A Pt wire and a saturated calomel electrode (SCE, Pine) were used as the counter and reference electrode, respectively. Argon was bubbled into the solution at 60 ml min^{-1} for 30 min to remove dissolved oxygen, followed by a continuous flow of 30 ml min^{-1} above the solution to form a gas curtain during the analysis.

Thin catalyst and Nafion films were casted on the GC-RDE sequentially as the working electrode [42]. Two 10 μl syringes (Hamilton, Gastight®) were used to add 1 $mg_{cat.}$ ml^{-1} catalyst aqueous solution and 100 times diluted 5 wt% Nafion on the GC-RDE. Both cast films were dried overnight at room temperature after each casting. The loading of the catalyst was 36 μg Pt cm^{-2} and the Nafion film was ca. 0.1 μm in thickness.

The working electrode potential was cycled 5 times between 0.05 and 1.4 V (vs. NHE) at a scan rate of 100 mV s^{-1} to remove slight contamination from the Nafion solution to get a clean electrode surface. Then it was cycled between 0.05 and 1.2 V (vs. NHE) at a scan rate of 100 mV s^{-1}. The working electrode potential was held at 0.1 V (vs. NHE) at idle time. Hydrogen desorption peak area was used to quantify the electrochemical surface area (ECSA). The area was integrated by the PineChem 2.8.0 (Pine Instrument) software.

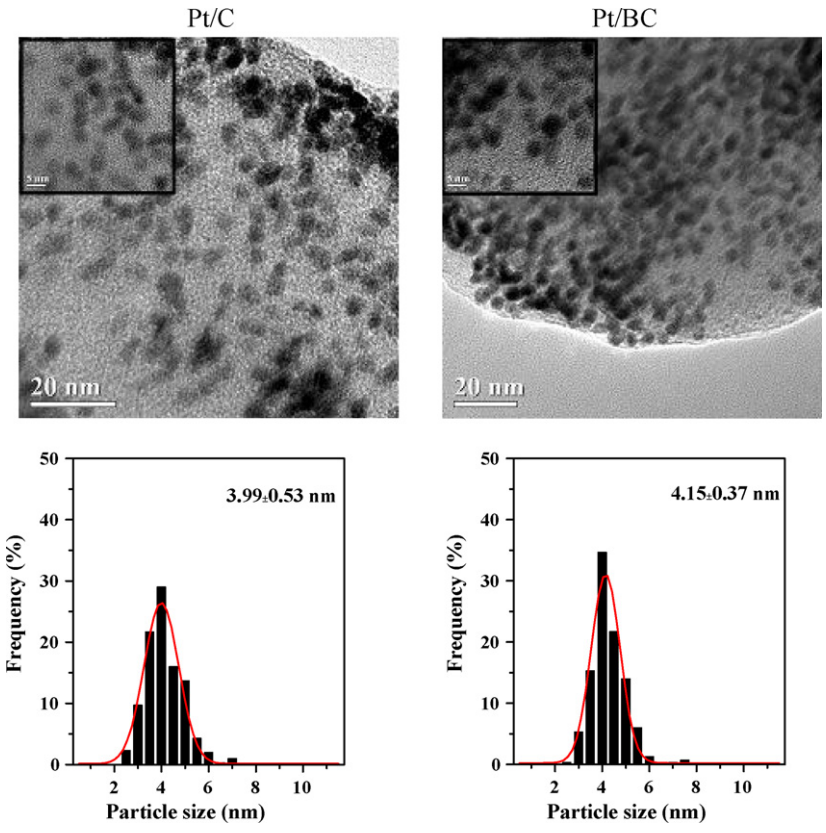

Fig. 2. TEM images of Pt nanoparticles on pure and boron-doped carbon supports.

3. Results and discussion

3.1. X-ray characterization of Pt/carbon

The average crystallite size of the Pt nanoparticles on the pure and boron-doped carbon supports is estimated to be 4 nm using the Scherrer equation [43] with the linewidth of the diffraction peaks in XRD curves (Fig. 1). From Fig. 1, it can be seen that the size of the boron-doped carbon was larger than the pure carbon because of the increased graphitization of the carbon caused by the presence of boron in the carbon lattice [34]. This lowered the BET surface area of the boron-doped carbon support from 21 $m^2\,g^{-1}$ (of the pure carbon) down to 12 $m^2\,g^{-1}$. It is acknowledged that these surface areas are significantly lower than what is required for most catalytic applications, so our current experimental efforts have been focused on tuning our synthesis method to produce high surface area supports. When the Pt nanoparticles were deposited on the supports, the BET surface area of the pure carbon-supported catalyst was 15 $m^2\,g^{-1}$, and the BET surface area of the boron-doped carbon-supported Pt catalyst was 7 $m^2\,g^{-1}$. The size of the Pt nanoparticles on pure and boron-doped carbon estimated from the XRD spectra was further confirmed by the TEM images of these systems shown in Fig. 2.

To understand the interactions between Pt and the supports, the Pt4f, C1s, and O1s spectra of the Pt nanoparticles on the pure and boron-doped carbon supports were obtained using XPS. The Pt4f peaks were deconvoluted into $Pt4f_{7/2}$ and $Pt4f_{5/2}$ doublets labeled as 1, 2, and 3, and 1′, 2′, and 3′, respectively, as shown in Fig. 3. The most intense doublet, namely the 1 and 1′, was located at 71.1 and 74.5 eV (for pure carbon), and 71.4 and 74.8 eV (for boron-doped carbon), respectively. This doublet can be attributed to metallic platinum. The second doublet, namely the 2 and 2′, was located at 72.3 and 76.1 eV (for pure carbon), and 72.6 and 76.4 eV (for boron-doped carbon), respectively. This doublet can be assigned to Pt(II) chemical states such as PtO and $Pt(OH)_2$ adsorbed on the nanoparticle. The third doublet, namely the 3 and 3′, was located at 73.8 and 79.7 eV (for pure carbon), and 74.1 and 80.0 eV (for boron-doped carbon), respectively. This doublet can be assigned to the higher chemical state functional groups such as PtO_2 and other Pt(IV) groups adsorbed on the metal nanoparticle [44–46]. However, Zhang et al. [47] have assigned the first, second, and third pair of doublets to metallic Pt on the surface, bulk Pt atoms, and PtO_x on the surface of the metal nanoparticle, respectively.

The Pt4f binding energy shift is a function of the size of the nanoparticle. Consequently, smaller Pt nanoparticles will shift the binding energy of the Pt4f peak towards higher binding energy [47]. However, the Pt nanoparticles on the pure and boron-doped carbon were of the same average size, as confirmed from the XRD and TEM analysis. Consequently, the shift of the Pt4f peak on the boron-doped carbon could not be attributed to differences in particle size. The shift in the Pt4f peak on the boron-doped carbon-supported catalyst is likely due to the modified interaction between the metal and the support. The binding energies of the Pt4f peaks on the boron-doped carbon increased by 0.3 eV when compared to the Pt4f peaks on the pure carbon. The boron in carbon lowers the Fermi energy of the support, which facilitates higher transfer of electrons from the Pt nanoparticles to the boron-doped carbon, as compared to the charge transfer from the Pt to the pure carbon, leading to a higher interaction between the Pt and boron-doped carbon [32,33]. This is reflected in the Pt4f doublets on the boron-doped carbon by shifting towards the higher energy level. These results are qualitatively consistent with our previous DFT calculations of model systems [31–33], which predict an enhancement of 0.6 eV. The calculation results should serve as an upper limit, since this prediction represents the adsorption energy of a *single* Pt atom.

The C1s envelope of the pure and boron-doped carbon was deconvoluted into three peaks as shown in Fig. 3. The three peaks labeled as 1, 2, and 3 (or C1, C2, and C3), were located at 284.8, 286.4, and 289.2 eV (for pure carbon), and 284.5, 286.6, and 289.9 eV (for boron-doped carbon), respectively. The C1 spectra of the pure and boron-doped carbon are due to the carbon support (graphitic carbon). The C2 and C3 peaks on both of the carbons are due to the presence of functional groups, such as –C=O, –C–OH, and –COOH, with different chemical states [26,44,47]. The C1s spectrum of the boron-doped carbon was broader than the C1s spectrum of the pure carbon. Zhang et al. [47] have also seen a broader C1s spectrum of the HOPG support when the interaction between the Pt nanoparticle and the support was higher, which is consistent with the broader C1s spectrum of our boron-doped carbon support.

The O1s spectra of the pure and boron-doped carbon were deconvoluted into two peaks as shown in Fig. 4. The peaks, labeled as 1 and 2, were located at 531.6 and 533.8 eV (for pure carbon) and 531.6 and 534.5 eV (for boron-doped carbon), respectively. The two peaks arise due to the functional groups on the carbon support [26,47]. The oxygen content in the boron-doped carbon-supported catalyst was higher than that of the oxygen content in the pure carbon-supported catalyst. In the boron-doped support, the oxygen preferentially attacks the boron, forming boron oxides, thus having an inhibiting effect on the carbon oxidation [48]. The boron oxides that are formed passivate the carbon surface, further inhibiting the oxidation of carbon. This can be beneficial for fuel cell electrode catalysts, since carbon corrosion is a major issue [30,46,49].

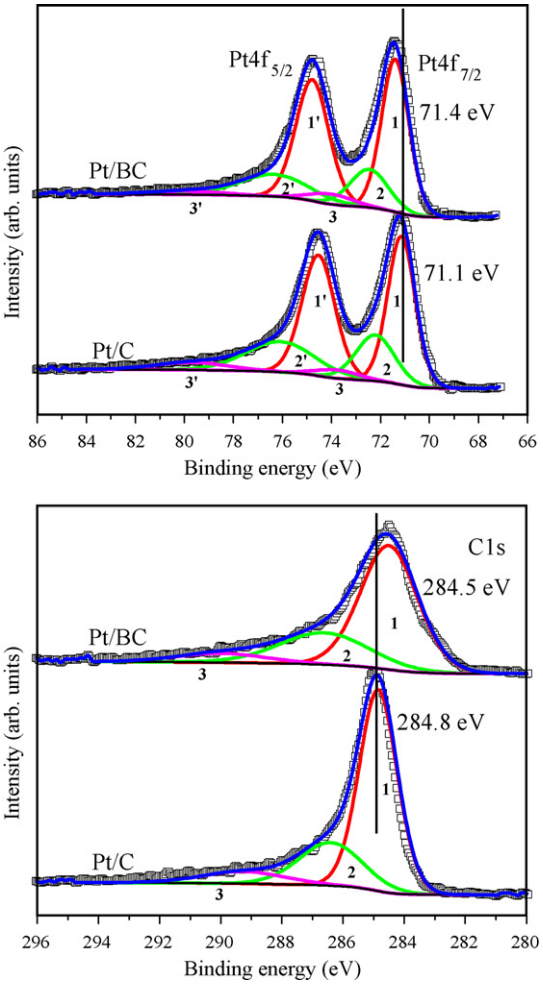

Fig. 3. Pt4f and C1s energy levels in the XPS spectra of the Pt nanoparticles on the pure and boron-doped carbon supports.

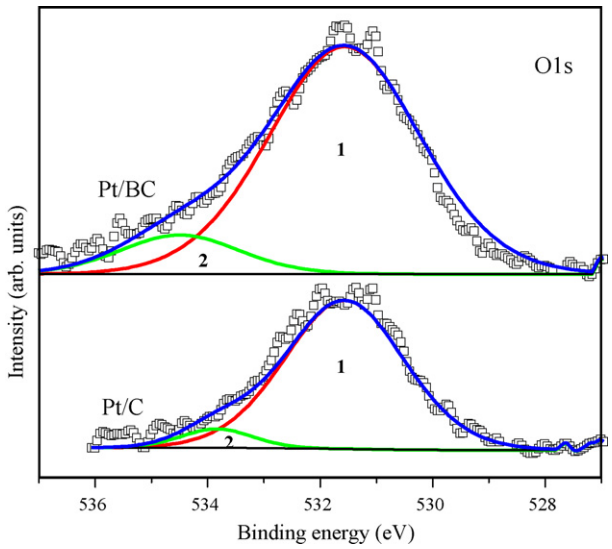

Fig. 4. O1s energy levels in the XPS spectra of the Pt nanoparticles on the pure and boron-doped carbon supports.

The XPS results indicate a higher interaction of the Pt nanoparticles with the boron-doped carbon when compared to the interaction of the Pt nanoparticles with the pure carbon. However, further studies are required to see if this difference in interaction between the Pt nanoparticles and the two carbon systems has any significance in catalytic and electrocatalytic reactions. If it has an influence on reactions, we would also like to study its limitations.

3.2. Electrochemical characterization of Pt/carbon

Carbon-supported platinum catalysts lose electrochemical surface area (ECSA) due to carbon support corrosion and Pt dissolution/aggregation. Continuous cycling of the potential from 50 mV to 1200 mV (vs. NHE) causes the catalysts to undergo iterative Pt dissolution and carbon corrosion, so as to accelerate the catalyst degradation. Fig. 5 shows the ECSA changes of Pt/C and Pt/BC catalysts with respect to the number of potential cycles. The ECSA of the Pt/C catalyst decreased faster than that of the Pt/BC catalyst, which means that the latter has a lower degradation rate and higher stability. This could be attributed to the lower carbon support corrosion and/or Pt dissolution/aggregation rates. On the other hand, the ECSA of both of the catalysts was shortly at a maximum and then started to decrease. The maximum ECSA of Pt/C is at about 50 cycles, which is lower than that of the Pt/BC catalyst, which occurred at around 100 cycles. This phenomenon is ascribed to the

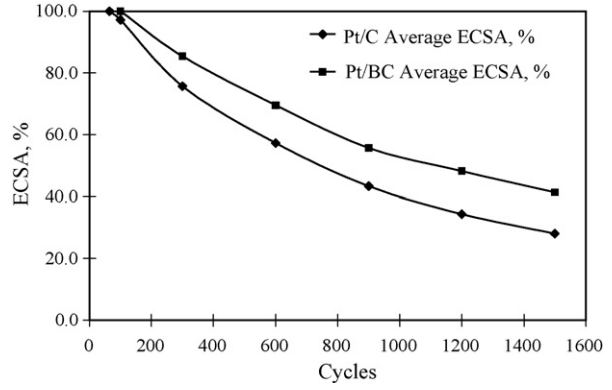

Fig. 5. Electrochemical surface area (ECSA) changes with potential cycles of the pure and boron-doped carbon-supported catalysts.

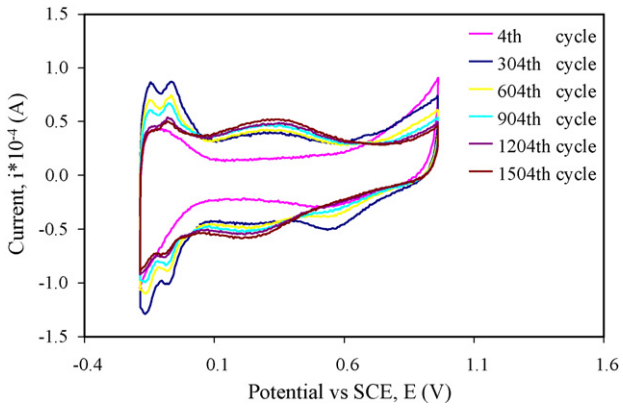

Fig. 6. Cyclic voltammetry changes with potential cycles on the pure carbon-supported Pt catalyst.

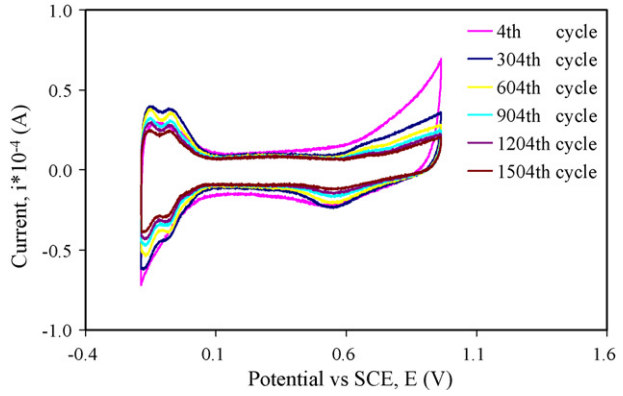

Fig. 7. Cyclic voltammetry changes with potential cycles on the boron-doped carbon-supported Pt catalyst.

electrocatalyst activation. Since the Pt/BC catalyst is more stable, it needs longer time to be activated and degrades slower than the Pt/C catalyst.

Figs. 6 and 7 show the Pt/C and Pt/BC CV curve changes with potential cycles, respectively. At a potential of around 0.35 V vs. SCE, there is a current peak due to the carbonaceous species oxidizing to CO_2 on the carbon support surface [27,50,51], which causes the carbon support to corrode. The carbon corrosion current in Fig. 6 for the Pt/C catalyst is much more significant than that for the Pt/BC catalyst, as shown in Fig. 7. As for the Pt/C catalyst, the current increased significantly with the increase in the potential cycle, which means that the carbon corrosion has accelerated. However, there is almost no carbon oxidation current for the Pt/BC catalyst, which implies that the Pt/BC catalyst undergoes less carbonaceous oxidation of the carbon support. These results are consistent with the XPS experimental results. The boron oxides that are formed passivate the carbon surface, further inhibiting the oxidation of carbon so as to decreases the carbon support corrosion rate.

4. Conclusions

In this work, 4.0 nm Pt nanoparticles were synthesized by chemical reduction of platinum acetylacetonate with the aid of oleylamine and oleic acid. The Pt nanoparticles were loaded on the two different carbon supports by physical deposition. The XPS results indicate that the interaction between the Pt nanoparticles and the boron-doped carbon support was higher than the interaction between the Pt nanoparticles and the pure carbon support. These experimental results are qualitatively consistent with our previous DFT calculations of model systems [31–33]. The XPS results

predict a binding energy enhancement of 0.3 eV on the doped carbon support, and our DFT calculations predict an enhancement of 0.6 eV (which should serve as an upper limit, since this prediction represents *single* Pt atom adsorption energy). The electrochemical results also suggest that the boron in carbon lowers the corrosion of the carbon support, which can be beneficial for the durability of fuel cell electrode catalysts, since carbon corrosion is a major issue.

Acknowledgements

Funding for this work was provided by DOE EPSCoR, Grant #DE-FG02-01ER45867. CHT acknowledges support from an NSF CAREER award (#0747690). This work used the Central Analytical Facility, which is supported by The University of Alabama.

References

[1] E. Auer, A. Freund, J. Pietsch, T. Tacke, Appl. Catal. A 173 (1998) 259–271.
[2] W.L. Holstein, H.D. Rosenfeld, J. Phys. Chem. B 109 (2005) 2176–2186.
[3] J. Kua, W.A. Goddard, J. Am. Chem. Soc. 121 (1999) 10928–10941.
[4] Q. Lu, B. Yang, L. Zhuang, J. Lu, J. Phys. Chem. B 109 (2005) 1715–1722.
[5] Y.Y. Tong, H.S. Kim, P.K. Babu, P. Waszczuk, A. Wieckowski, E. Oldfield, J. Am. Chem. Soc. 124 (2002) 468–473.
[6] T. Frelink, W. Visscher, J.A.R. van Veen, J. Electroanal. Chem. 382 (1995) 65–72.
[7] H. Chunzhi, H.R. Kunz, J.M. Fenton, J. Electrochem. Soc. 144 (1997) 970–979.
[8] T. Kawaguchi, W. Sugimoto, Y. Murakami, Y. Takasu, J. Catal. 229 (2005) 176–184.
[9] L. Seol-Ah, P. Kyung-Won, C. Jong-Ho, K. Boo-Kil, S. Yung-Eun, J. Electrochem. Soc. 149 (2002) A1299–A1304.
[10] S. Mukerjee, J. McBreen, J. Electroanal. Chem. 448 (1998) 163–171.
[11] R. Narayanan, M.A. El-Sayed, Nano Lett. 4 (2004) 1343–1348.
[12] S. Park, S.A. Wasileski, M.J. Weaver, J. Phys. Chem. B 105 (2001) 9719–9725.
[13] M. Bowker, Nat. Mater. 1 (2002) 205–206.
[14] C. Alonso, R.C. Salvarezza, J.M. Vara, A.J. Arvia, L. Vazquez, A. Bartolome, A.M. Baro, J. Electrochem. Soc. 137 (1990) 2161–2166.
[15] I. Lee, K.-Y. Chan, D.L. Phillips, Appl. Surf. Sci. 136 (1998) 321–330.
[16] L. Bardotti, P. Jensen, A. Hoareau, M. Treilleux, B. Cabaud, Phys. Rev. Lett. 74 (1995) 4694–4698.
[17] P. Jensen, Rev. Mod. Phys. 71 (1999) 1695–1735.
[18] P. Jensen, A. Clement, L.J. Lewis, Comput. Mater. Sci. 30 (2004) 137–142.
[19] D.Q. Yang, G.X. Zhang, E. Sacher, M. Jose-Yacaman, N. Elizondo, J. Phys. Chem. B 110 (2006) 8348–8356.
[20] A. Masson, J.J. Metois, R. Kern, Surf. Sci. 27 (1971) 463–482.
[21] S.-P. Huang, P.B. Balbuena, Mol. Phys. 100 (2002) 2165–2174.
[22] H. Tachikawa, A. Shimizu, J. Phys. Chem. B 109 (2005) 13255–13262.
[23] G. Lu, G. Zangari, Electrochim. Acta 51 (2006) 2531–2538.
[24] P. Melinon, A. Hannour, B. Prevel, L. Bardotti, E. Bernstein, A. Perez, J. Gierak, E. Bourhis, D. Mailly, J. Cryst, Growth 275 (2005) 317–324.
[25] S. Lee, H. Permana, K.Y.S. Ng, J. Vac. Sci. Technol. B 10 (1992) 561–565.
[26] D.Q. Yang, E. Sacher, Chem. Mater. 18 (2006) 1811–1816.
[27] K. Kinoshita, Carbon: Electrochemical and Physicochemical Properties, Wiley, New York, 1988.
[28] H. Binder, A. Köhling, K. Richter, G. Sandstede, Electrochim. Acta 9 (1964) 255–274.
[29] A. Casalegno, R. Marchesi, J. Power Sources 175 (2008) 372–382.
[30] R. Borup, J. Meyers, B. Pivovar, Y.S. Kim, R. Mukundan, N. Garland, D. Myers, M. Wilson, F. Garzon, D. Wood, P. Zelenay, K. More, K. Stroh, T. Zawodzinski, J. Boncella, J.E. McGrath, M. Inaba, K. Miyatake, M. Hori, K. Ota, Z. Ogumi, S. Miyata, A. Nishikata, Z. Siroma, Y. Uchimoto, K. Yasuda, K.I. Kimijima, N. Iwashita, Chem. Rev. 107 (2007) 3904–3951.
[31] C.K. Acharya, C.H. Turner, J. Phys. Chem. B 110 (2006) 17706–17710.
[32] C.K. Acharya, D.I. Sullivan, C.H. Turner, J. Phys. Chem. C 112 (2008) 13607–13622.
[33] C.K. Acharya, C.H. Turner, J. Phys. Chem. C 111 (2007) 14804–14812.
[34] J.S. Burgess, C.K. Acharya, J. Lizarazo, N. Yancey, B. Flowers, G. Kwon, T. Klein, M. Weaver, A.M. Lane, C.H. Turner, S. Street, Carbon 46 (2008) 1711–1717.
[35] Z. Liu, E.T. Ada, M. Shamsuzzoha, G.B. Thompson, D.E. Nikles, Chem. Mater. 18 (2006) 4946–4951.
[36] Z. Liu, D. Reed, G. Kwon, M. Shamsuzzoha, D.E. Nikles, J. Phys. Chem. C 111 (2007) 14223–14229.
[37] Z. Liu, M. Shamsuzzoha, E.T. Ada, W.M. Reichert, D.E. Nikles, J. Power Sources 164 (2007) 472–480.
[38] V. Salgueirino-Maceira, L.M. Liz-Marzan, M. Farle, Langmuir 20 (2004) 6946–6950.
[39] M.P. Seah, I.S. Gilmore, G. Beamson, Surf. Interface Anal. 26 (1998) 642–649.
[40] P. Chen, H.B. Bhandari, T.M. Klein, Appl. Phys. Lett. 85 (2004) 1574–1576.
[41] B.J. Bachman, M.J. Vasile, J. Vac. Sci. Technol. A 7 (1989) 2709–2716.
[42] U.A. Paulus, T.J. Schmidt, H.A. Gasteiger, R.J. Behm, J. Electroanal. Chem. 495 (2001) 134–145.
[43] B.D. Cullity, Elements of X-Ray Diffraction, second ed., Addison–Wesley, MA, 1978.
[44] Z. Liu, L.M. Gan, L. Hong, W. Chen, J.Y. Lee, J. Power Sources 139 (2005) 73–78.
[45] A.K. Shukla, M.K. Ravikumar, A. Roy, S.R. Barman, D.D. Sarma, A.S. Arico, V. Antonucci, L. Pino, N. Giordano, J. Electrochem. Soc. 141 (1994) 1517–1522.
[46] J. Wang, G. Yin, Y. Shao, S. Zhang, Z. Wang, Y. Gao, J. Power Sources 171 (2007) 331–339.
[47] G. Zhang, D. Yang, E. Sacher, J. Phys. Chem. C 111 (2007) 565–570.
[48] L.R. Radovic, M. Karra, K. Skokova, P.A. Thrower, Carbon 36 (1998) 1841–1854.
[49] M. Cai, M.S. Ruthkosky, B. Merzougui, S. Swathirajan, M.P. Balogh, S.H. Oh, J. Power Sources 160 (2006) 977–986.
[50] L.M. Roen, C.H. Paik, T.D. Jarvi, Electrochem. Solid-State Lett. 7 (2004) A19–A22.
[51] S. Maass, F. Finsterwalder, G. Frank, R. Hartmann, C. Merten, J. Power Sources 176 (2008) 444–451.